Temporal and spectral signatures of the interaction between ultrashort laser pulses and Bloch surface waves

APL Photonics

RESEARCH ARTICLE | APRIL 05 2024

Temporal and spectral signatures of the interaction between ultrashort laser pulses and Bloch surface waves

Isaac Doughan ; Atsu L. Asilevi ; Atri Halder ; Tian-Long Guo ; Erika Mogni ; Michele Celebrano ; Marco Finazzi ; Giovanni Pellegrini ; Paolo Biagioni ; Emiliano Descrovi ; Matthieu Roussey ; Jari Turunen

APL Photonics 9, 046106 (2024)
https://doi.org/10.1063/5.0183704

Temporal and spectral signatures of the interaction between ultrashort laser pulses and Bloch surface waves

Cite as: APL Photon. 9, 046106 (2024); doi: 10.1063/5.0183704
Submitted: 24 October 2023 • Accepted: 19 March 2024 •
Published Online: 5 April 2024

Isaac Doughan,[1] Atsu L. Asilevi,[1,a)] Atri Halder,[1] Tian-Long Guo,[1] Erika Mogni,[2] Michele Celebrano,[2] Marco Finazzi,[2] Giovanni Pellegrini,[3] Paolo Biagioni,[2] Emiliano Descrovi,[4] Matthieu Roussey,[1,b)] and Jari Turunen[1]

AFFILIATIONS

[1] Center for Photonics Sciences, Department of Physics and Mathematics, University of Eastern Finland, P.O. Box 111, 80101 Joensuu, Finland
[2] Dipartimento di Fisica, Politecnico di Milano, Piazza Leonardo da Vinci 32, 20133 Milano, Italy
[3] Dipartimento di Fisica, Università di Pavia, via Bassi 6, 27100 Pavia, Italy
[4] Dipartimento di Scienza Applicata e Tecnologia, Politecnico di Torino, 10129 Torino, Italy

[a)] **Electronic mail:** lewisa@uef.fi
[b)] **Author to whom correspondence should be addressed:** matthieu.roussey@uef.fi

ABSTRACT

The resonant excitation of Bloch Surface Waves (BSWs) in dielectric one-dimensional photonic crystals is becoming a realistic photonic solution for surface integration in many domains, from spectroscopy to local field management. Bringing BSWs to ultrafast and nonlinear regimes requires a deep knowledge of the effects that the photonic crystal dispersion and the resonant surface wave excitation have on the ultrashort laser pulses. We report on the experimental evidence of spectral and temporal modifications of the radiation leaving a planar one-dimensional photonic crystal after coupling to BSWs. In such a resonant condition, a characteristic long temporal tail is observed in the outgoing pulses. Observations are performed by employing both frequency-resolved optical gating and field cross-correlation techniques.

Bloch surface waves (BSWs) are either transverse electric (TE)- or transverse magnetic (TM)-polarized evanescent modes mostly confined at the surface of a periodically stratified dielectric medium (a one-dimensional photonic crystal), topped with a suitable termination layer.[1–4] In high-transparency materials, BSWs can propagate along the multilayer surface over lengths in the millimeter and even centimeter range,[5] with radiation leakage through the substrate being one of the most severe sources of loss. When excited by means of an external radiation incident on the multilayer through a high-refractive index substrate, BSWs manifest themselves as reflectivity dips whose spectral and angular positions are reminiscent of the mode dispersion in energy and momentum, respectively. Due to their highly confined nature, they find key applications, for instance, in surface-enhanced sensing, where they have been demonstrated to compete with the performance of more established surface plasmon resonance techniques.[6,7] In previous studies, continuous-wave illumination has been mainly employed to investigate BSWs, although a few short-pulse illumination schemes have also been proposed. For example, one can find studies on nonlinear effects driven by BSWs, such as ultrafast switching[8] and self-action.[9] More recently, modifications in the temporal profile of short light pulses emerging from a dielectric multilayer after resonant coupling to BSWs have been theoretically investigated by some of the authors.[10] There, the complex transmission coefficient of BSWs is found to follow a Lorentz-type spectral curve with rapid variations in both amplitude and phase about the resonance frequency. Translated to the time domain, this means that each reflected pulse exhibits an initial peak followed by a delayed tail, which is caused by the dispersive response

of the photonic crystal. However, no direct evidence of such an effect has been reported so far. In this paper, we report on the experimental observation of such a phenomenon, i.e., the wavelength-dependent temporal profile of short pulses leaving a planar dielectric multilayer after BSW coupling. After introducing the multilayer geometry and the related optical characterizations, we provide evidence of the spectral–temporal reshaping of the pulse. Time-domain measurements of short pulses upon BSW coupling are shown using two methods: frequency-resolved optical gating (FROG)[11] and linear field cross-correlation measurements.[12] In both types of measurements, we observed a clear time-separation between different portions of the collected pulses, respectively related to the reflected radiation from the multilayer and the leakage radiation from coupled BSWs. As these two components are often spatially overlapped, the possibility of performing a selective detection based on time-gating opens interesting opportunities for background reduction in optical sensing based on surface and guided modes in planar structures.

Figure 1(a) illustrates the structure considered here and the related BSW coupling mechanism. The multilayer is constituted by a stack of four TiO_2 and SiO_2 bilayers topped with an additional TiO_2 layer to finely tune the spectral position of the BSW, as shown in the cross section imaged at the scanning electron microscope in Fig. 1(b). Growth of dielectrics is performed by plasma-enhanced atomic layer deposition (PE-ALD, TFS-200, Beneq)[13] on a glass substrate (Corning, refractive index $n_s = 1.518$ at $\lambda_0 = 800$ nm). In particular, TiO_2 layers were deposited with $TiCl_4$ and O_2 gases as precursors, while SiO_2 thin films were made with bis(ethylmethylamino)silane (BEMAS) and O_2 gases. The nitrogen remote plasma power was 100 W for both processes. For both materials, we set the temperature at 150 °C.[14] The growth temperature has a significant effect on the refractive index of TiO_2, in particular, but also on the homogeneity and crystalline structure of the materials. Such a process temperature ensures the deposition of isotropic (amorphous) media.[15] The complex, frequency-dependent refractive indices of the dielectric materials were measured by variable angle spectroscopic ellipsometry (VASE).[16] For example, we measured $n_H = 2.316$ for TiO_2 and $n_L = 1.450$ for SiO_2 at $\lambda_0 = 800$ nm wavelength.

The nominal thicknesses of the dielectric layers are designed to have a sharp TE-polarized BSW mode in the near-infrared spectral range, at about 800 nm wavelength. As a first step, the one-dimensional photonic crystal is characterized by continuous-wave illumination by both normal incidence reflectivity measurements, exploiting the incoherent white light source from the ellipsometric setup, and by angular scans at fixed wavelengths in the Kretschmann configuration, exploiting diode laser sources at wavelengths $\lambda = 706$ and 790 nm. The Kretschmann configuration setup requires the bottom side of the glass substrate carrying the dielectric multilayer to be oil-contacted to a right-angle glass prism. The results of both measurements are presented in Fig. 2 and compared with calculations. While the normal-incidence spectrum [Fig. 2(a)] is substantially influenced by the overall photonic-crystal stack, the angular scans [Fig. 2(b)] highlight the excitation of the BSW modes, whose energy-momentum position is strongly dependent on the refractive index and thickness of the termination layer.

Experimental reflectivity measurements allow us to give feedback on our simulations to determine the thickness of the dielectric

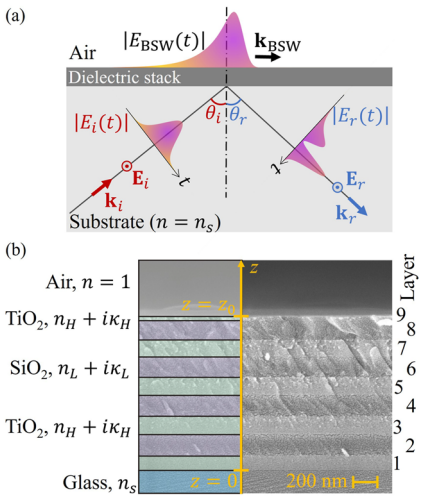

FIG. 1. Geometry and notations. (a) Illumination and collection scheme for BSW excitation by means of an expanded Gaussian pulsed beam. The prism and optical setup used for the excitation are not represented. (b) Cross-sectional sketch of the multilayer superimposed on an SEM picture of the stack.

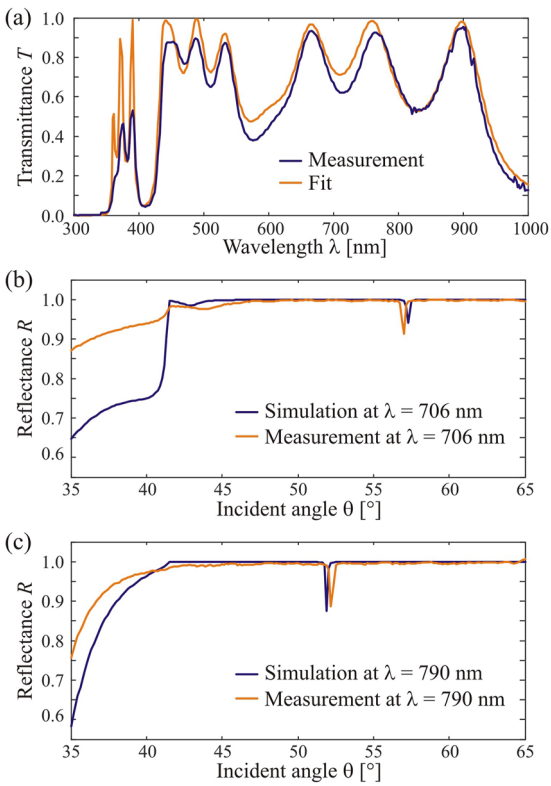

FIG. 2. Multilayer reflectivity. (a) Comparison between calculated and measured spectral transmittance at normal incidence. [(b) and (c)] Calculated and measured (blue and orange, respectively) angular reflectance at 706 nm (b) and 790 nm (c) wavelengths.

TABLE I. Geometrical parameters of the dielectric multilayer. We consider at $\lambda = 800$ nm the following refractive indices (listed from bottom to top, as shown in Fig. 1): for the high refractive index layers TiO_2, $n_H = 2.316$ and $\kappa_H = 1 \times 10^{-4}$, and for the low refractive index layers SiO_2, $n_L = 1.450$ and $\kappa_L = 1 \times 10^{-5}$.

Layer	1	2	3	4	5	6	7	8	9
Material	TiO_2	SiO_2	TiO_2	SiO_2	TiO_2	SiO_2	TiO_2	SiO_2	TiO_2
t (nm)	107.2	176.4	124.1	189.0	136.7	190.4	152.1	172.6	20.5

layers. To reproduce the experimental measurements, we fit the normal-incidence reflectivity data by coupling a genetic differential evolution algorithm to a traditional transfer matrix formalism.[17,18] The system evolves for 800 generations, considering all layer thicknesses as free parameters. After this first step, the thickness of the termination layer, which has negligible impact on the normal-incidence reflectivity, is empirically determined to reproduce the angular position of the BSWs measured at $\lambda = 706$ and 790 nm; see Figs. 2(b) and 2(c). This leads to an accurate fit and realistic geometrical parameters, as summarized in Table I.

For time-resolved characterizations, illumination in the Kretschmann configuration is provided by a collimated Gaussian pulsed laser beam from a femtosecond laser source cascaded with an optical parametric amplifier (PHAROS and ORPHEUS, from Light Conversion). We set the polarization state as transverse electric (TE) in order to match the sharper BSW mode sustained by the multilayer. In Appendix A, details on the laser pulse characteristics are reported. Analytically, the electric field of the illumination beam can be expressed in the time domain and its Fourier transform in the frequency domain, respectively, as

$$E(t) = A_0 \exp\left(-\frac{t^2}{T^2}\right)\exp\left(-i\omega_0 t\right) \tag{1}$$

and

$$E(\omega) = E_0 \exp\left[-\frac{(\omega-\omega_0)^2}{\Omega^2}\right], \tag{2}$$

where the amplitude E_0 is assumed to be constant, $\omega_0 = 1.7$ rad/fs ($\lambda_0 = 2\pi c/\omega_0 = 800$ nm) is the central frequency, $\Omega = 2.7063 \times 10^{13}$ rad/s is the frequency bandwidth, and $T = 2/\Omega$ is the time domain half width at E_0/e. The term $A_0 = \sqrt{\pi}\Omega E_0$ is used for normalization.

First, we characterize the reflected pulse in amplitude and phase via second-harmonic frequency-resolved optical gating (SHG-FROG). In this well-established SHG-FROG method, a two-dimensional spectrogram (a signal generated via the SHG process) $G(\omega,\tau) = |F(\omega,\tau)|^2$ is recorded, where

$$F(\omega,\tau) = \int_{-\infty}^{\infty} E(t)E(t-\tau)\exp\left(i\omega t\right)\mathrm{d}t, \tag{3}$$

and a pulse shape retrieval algorithm (also known as the FROG algorithm) is used to retrieve the amplitude and phase of the laser pulse under investigation, both in the spectral and temporal domains.[11] However, as it will become clearer later on, SHG-FROG does not possess the sensitivity to characterize the weak temporal tail of the reflected pulse. Therefore, in a second experiment, we turned to cross-correlation measurements and characterized the temporal pulse behavior via linear interferometry.

In the first experiment, we employ a θ–2θ goniometric setup constituted by two computer-controlled rotation stages to adjust the illumination and the detection at the (internal) angles of incidence and reflection to θ_i and $\theta_r = 2\theta_i$, respectively. A wavelength-selective detection is performed along the reflection path [Fig. 3(a)] by employing a custom dispersive spectrometer with a 1 mm-wide entrance slit, a reflective diffraction grating (Thorlabs GR25-0305, 300 lines/mm), a cylindrical positive lens with a focal length of 10 cm, and a CMOS camera (Thorlabs DCC1545M). When needed,

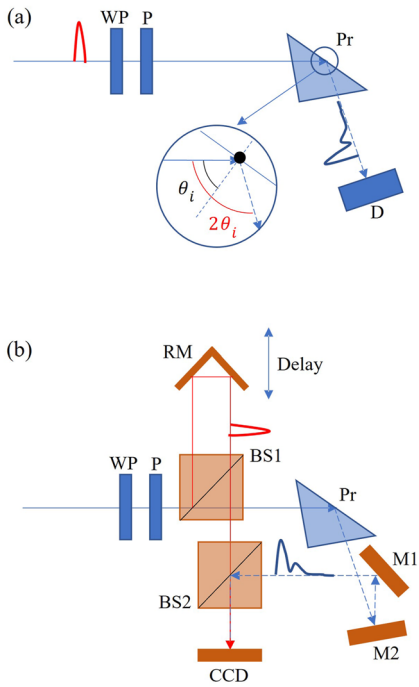

FIG. 3. Schematic of the experimental setup used for (a) angularly and spectrally resolved reflected intensity and FROG measurement and (b) cross-correlation amplitude measurement. Here, WP = half wave plate, P = linear polarizer, Pr = prism, D = detector, RM = roof mirror, BS1 and BS2 are 50:50 non-polarizing beam splitters, M1 and M2 are plane mirrors, and CCD is the camera. The rotation axis is indicated by the black dot on the prism's long side, and the internal angle of incidence is θ_i.

the detector was replaced by a second harmonic (SHG) frequency resolved optical gating (FROG) device.

The setup above is then modified in order to collect pulse time traces through cross-correlation amplitude measurements [Fig. 3(b)]. More specifically, a delay line is introduced between the incident and reflected radiation, and the detection is performed by means of a CCD camera (Thorlabs DCC1545M). First, we use a non-polarizing 50:50 beam-splitter, BS1, to produce an object and a reference beam with equal intensity. Next, we rotate the prism carrying the sample with respect to the object beam to match the incidence angle corresponding to the BSW resonance at the 800 nm wavelength. The reflected pulse from the sample is then directed onto a second beam-splitter, BS2, by means of two mirrors, M1 and M2. The reference beam propagates through a delay line, gets reflected by the upper mirror RM, and is superimposed on the reflected (object) beam at BS2. When the two pulses are temporally superimposed, a spatial interference fringe pattern is produced on the camera plane. The visibility of the interference fringes is then estimated as a function of the delay. The relationship between fringe visibility and the (normalized) envelope of the cross-correlation signal is illustrated in Appendix B.

Using the same setup, one can also measure the auto-correlation signal of the original laser pulse, which is achieved by setting off-resonance conditions either by changing the angle of incidence θ_i or switching to TM polarization, as no TM modes are available in the spectral and angular range considered. In either case, the reflected pulse can be safely assumed to be representative of the incident pulse since the dispersion introduced by the glass elements is negligible for the employed pulse time duration. After measuring the auto-correlation function, the spectral and temporal characteristics of the original laser pulse can thus be retrieved. Finally, a comparison between the auto-correlation and the cross-correlation signals would provide a clear signature of the pulse modulation produced by the resonant BSW excitation.

Calculated and measured maps for the reflected intensity $I_R(\lambda, \Delta\theta)$ are, respectively, shown in Figs. 4(a) and 4(b), where $\Delta\theta$ is calculated from the BSW coupling angle θ_{BSW} at the reference wavelength λ = 800 nm.

The coupling of BSW is visible as a narrow dip that is angularly and spectrally distributed according to the BSW dispersion. As an example, in Fig. 4(c), the measured reflected intensity spectrum at $\theta_i \approx 49.75°$ is also shown, together with the spectrum of the incident pulse and the calculated spectrum of the reflected beam extrapolated from the SHG-FROG data. Note that in Fig. 4, the calculated map has been angularly shifted (by less than 2°) in order to reproduce the experimental data. While this has no impact whatsoever on the physical interpretation of the observed phenomena, it compensates for slight alignment issues in the different setups employed for the continuous-wave (Fig. 2) and time-resolved (Fig. 4) measurements.

The time traces of the reflected radiation after resonant BSW excitation are measured by introducing the FROG device along the reflection path. We used second-harmonic FROG UPM-8-50 (a GRENOUILLE implementation see Chap. 12 in Ref. 11) for this purpose. The measured FROG spectrogram of the reflected pulse is shown in Fig. 5(a), together with the one reconstructed using the results of the retrieval algorithm that extracts the amplitude and phase of the laser pulse [Fig. 5(b)]. Their wing-like shape is a manifestation of the long, decaying secondary tail in the reflected pulse, as we will discuss later.

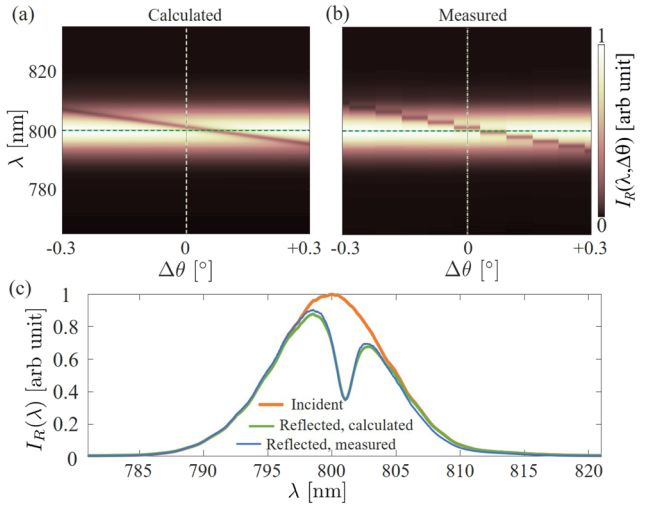

FIG. 4. Calculated (a) and measured (b) dispersion maps (reflectance) around the resonance wavelength λ = 800 nm. BSW is observed as a dispersed dip in the reflected intensity. The considered spectral range is determined by the incident pulse bandwidth. For better visibility, the angular response is referenced to the excitation angle as $\Delta\theta = \theta_i - \theta_{BSW}$, where θ_{BSW} is the angular position of the BSW dip at a wavelength of 800 nm. (c) Calculated (green solid curve) and measured (blue solid curve) reflected intensity profiles of incident light (orange solid curve).

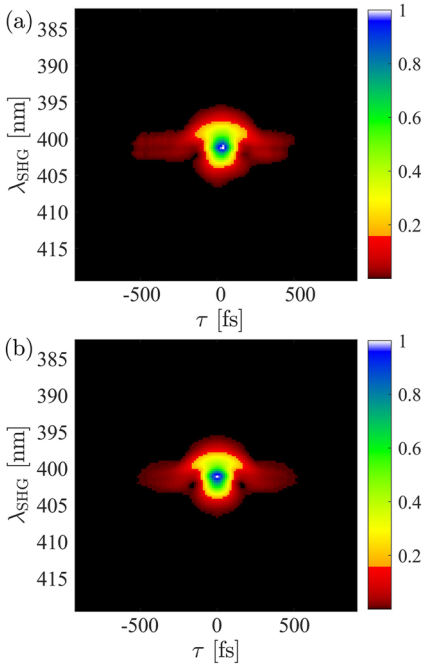

FIG. 5. (a) Measured and (b) retrieved FROG spectrograms with $N \times N$ = 128 × 128 pixel resolution (FROG error of 0.004).

A FROG error (i.e., the rms difference between the measured and retrieved normalized FROG spectrograms) of 0.004 demonstrates the good convergence of the retrieval algorithm, which can also be visually seen in Fig. 5. Moreover, comparing the spectrogram of the reflected pulse (as in Fig. 5) with that of the incident pulse (see Appendix A), one can appreciate the effect of the resonant BSW excitation on the reflected pulse.

Figure 6 shows the retrieved absolute values of the electric field amplitude and phase profiles of the reflected pulses in both the spectral (a) and temporal (b) domains. For comparison, we also plotted the simulated electric field amplitude and phase profiles in Figs. 6(c) and 6(d), in fair agreement with the experimental data. In all cases, the field profiles are normalized by the peak amplitude values. Again, a comparison of the reflected pulse profiles with the incident pulse profiles (see Appendix A) clearly indicates the BSW excitation and the associated pulse shape modulation.

In the spectral domain, the phase jump around a wavelength of 800 nm is also a clear signature of the resonance. In the time domain, the narrow BSW resonance modulates the laser pulse characteristics, and the spectral phase modulation determines a temporal broadening, splitting the pulse into two parts as shown by the dip around $t = 100$ fs that can be observed for both the simulated and retrieved pulse profiles. However, the FROG setup fails to accurately measure the long exponential temporal tail of the reflected pulse since the SHG signal significantly weakens because of its intrinsic nonlinear dependence on the input electric field amplitude. Note that we have used a simplified commercial version of the FROG device, called the GRENOUILLE. The retrieval codes are also optimized (in the available software) for the optical setting of the GRENOUILLE device we used. Therefore, no pre-processing has been employed to modify or possibly improve the quality of the extracted information from the tails. Moreover, the device can measure pulses with FWHM 50–300 fs wide with high accuracy; therefore, we are at the limit of our GRENOUILLE device.

For this reason, in order to reinforce the analysis, we further measure the cross-correlation signal between the incident and the reflected BSW pulses. In a recently introduced cross-correlation measurement scheme,[12] a similar experimental setup was used to measure the spectral coherence property of a supercontinuum field. However, in this work, we use a similar (but not the same) measurement setup for estimating pulse-shape. Figure 7(a) is a two dimensional map of the cross-correlation signal calculated as a function of $\delta\omega$ and $\Delta\tau$. The on-resonance (BSW mode) regime corresponds to $\delta\omega = 0$. The envelope of the measured cross-correlation signal is plotted as a red line in Fig. 7(b). For comparison, the theoretical cross-correlation signal (calculated as described in Ref. 10) is overlayed in the same figure (red line).

The measured cross-correlation curve exhibits a long-tailed portion of the signal peaked at about 0.2 ps delay that is less prominent as compared to the calculated one (dashed blue line). This delayed portion of the pulse is related to leakage radiation from BSWs. More specifically, the delayed signal in the collected pulse is ascribed to that part of the incident radiation that first couples to BSW, then propagates on the multilayer surface, and finally leaks

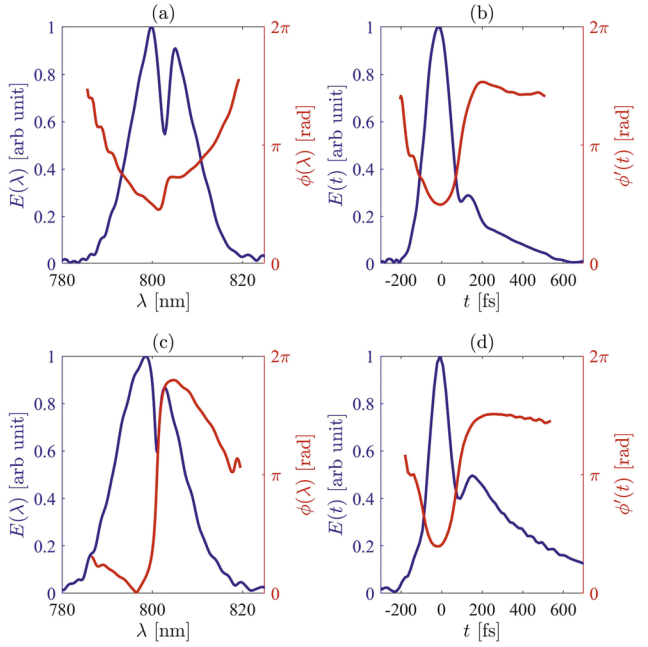

FIG. 6. Measured spectral (a) and temporal (b) field (blue solid) and phase (red solid) profiles. The phase is plotted against the right (red) axis and in the range where the spectral density or intensity is significant. The corresponding calculated spectral (c) and temporal (d) field and phase profiles are also plotted for comparison.

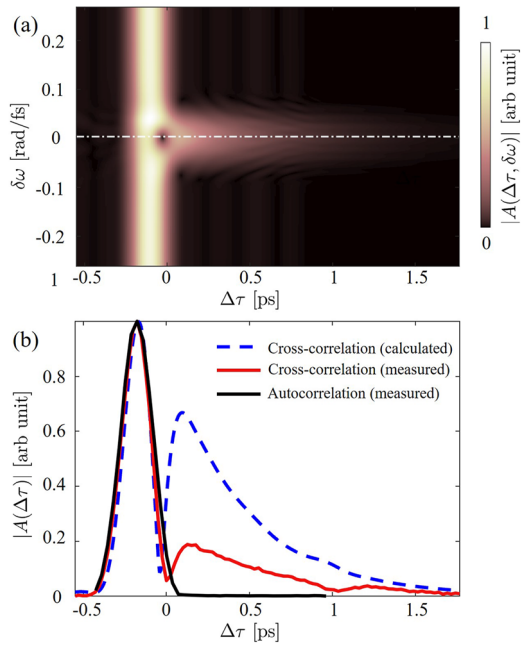

FIG. 7. (a) Calculated interference fringe visibility (cross-correlation) as a function of the delay ($\Delta\tau$) in picoseconds and the frequency shift $\delta\omega$. (b) Calculated (dashed blue) and measured temporal dependence of the reflected beam and measured autocorrelation in black.

into the glass substrate. Such leakage radiation follows a longer optical path with respect to the radiation that is directly reflected at the multilayer bottom, thus explaining the observed delay. Similarly to other guided modes on planar films, including surface plasmons, leakage radiation can be spatially overlapped with the reflected beam. The extent of such a spatial overlap depends on the divergence of the illumination beam and the propagation length of the guided mode. If the leakage radiation extends spatially beyond the reflected beam footprint, it might be partially cutoff from the collection optics, thus explaining a weaker intensity corresponding to the detected delayed peak. Another effect underlying the observed discrepancy between calculations and measurements can be found in the spectral phase profile of the detected pulses. In Figs. 6(a) and 6(c), a mismatch between measured and simulated spectral phase profiles can be observed. Such a mismatch may arise from complex light–matter interaction processes caused by, e.g., inhomogeneities of the layered materials, absorption, and has a direct impact on the retrieved temporal profile, therefore affecting the cross-correlation function.

As a cross-check, when we move off resonance by changing the polarization state of the incident pulse to TM, we measure the autocorrelation of the incident pulse [black line in Fig. 7(b)]. In this case, as expected, the temporal tail disappears. For completeness, in Fig. 7(a), we also show the whole calculated cross-correlation map displaying the pulse temporal behavior as a function of the detuning between the excitation and the resonance frequency. It is worth recalling that self-phase modulation due to nonlinear light–matter interaction may also result in an instantaneous frequency shift and, thus, split the intensity spectrum.[19] However, that is certainly not the case here, as the observed spectral splitting occurs even at very low incident pulse energies. Moreover, as the polarization state of the incident pulse is moved from the TE to the TM configuration, the original temporal structure of the incident pulse is recovered.

In conclusion, we employed FROG and cross-correlation measurements to experimentally characterize the modulation of ultrashort laser pulses in a Kretschmann configuration after the resonant excitation of BSWs, providing direct and definitive confirmation of the theoretical predictions previously published.[10] The richer amplitude and phase information provided by FROG is counterbalanced by lower sensitivity to the weak and long temporal tails introduced by the BSW excitation. Linear cross-correlation measurements, on the other hand, albeit delivering only amplitude information, are demonstrated to be the ideal probe for such long tails.

The combination of the two measurement techniques employed in this work offers, therefore, a new paradigm to benchmark ultrafast and nonlinear phenomena occurring at the surface of one-dimensional photonic crystals after BSW excitation and points to the non-negligible effects that BSW resonances have on the spectral and temporal characteristics of ultrashort pulses. In particular, the appearance of an amplitude dip in the spectral domain, associated with a step in the spectral phase, is a clear signature of the mode resonance and results in the appearance of the above-mentioned temporal tail, which is associated with leakage radiation from BSW. In this respect, the extension of time-resolved and nonlinear techniques to the domain of surface-enhanced spectroscopies employing BSWs can open new opportunities for optical sensing. As an example, properly time-gated detection could allow a selective collection of those portions of signal carrying the relevant information on the interaction between the coupled surface mode and the outer medium.

ACKNOWLEDGEMENT

The work was funded by the Research Council of Finland (Project No. 333938 and the Flagship Program PREIN, Project No. 346518). M.C. and M.F. acknowledge the partial financial support from the European Union's Horizon 2020 Research and Innovation program "METAFAST" (Grant Agreement No. 899673) and from the Italian Ministry of University and Research through the PRIN project NOMEN (Project No. 2017MP7F8F).

AUTHOR DECLARATIONS

Conflict of Interest

The authors have no conflicts to disclose.

Author Contributions

A.L.A. performed the time-resolved calculations and measurements and analyzed the experimental data; I.D. and A.H. designed and build the ultrafast characterization setup, performed the related measurements, and analyzed the measured data; T.-L.G. fabricated the samples and performed ellipsometric and SEM measurements; E.M., M.C., M.F., and P.B. performed the continuous-wave characterization of the BSW modes; G.P. performed the fitting analysis to model the continuous-wave results; E.D. contributed to the theory development and the overall analysis of the results; M.R. supervised the work and contributed to the analysis of the results; J.T. supervised the work and developed the theory. All authors contributed to the scientific discussion and the manuscript preparation.

Isaac Doughan: Data curation (equal); Formal analysis (equal); Methodology (equal); Writing – original draft (equal); Writing – review & editing (equal). **Atsu L. Asilevi**: Data curation (equal); Formal analysis (equal); Methodology (equal); Software (equal); Writing – original draft (equal); Writing – review & editing (equal). **Atri Halder**: Data curation (equal); Formal analysis (equal); Methodology (equal); Writing – original draft (equal); Writing – review & editing (equal). **Tian-Long Guo**: Data curation (equal); Formal analysis (equal); Writing – original draft (equal); Writing – review & editing (equal). **Erika Mogni**: Data curation (equal); Formal analysis (equal); Methodology (equal); Validation (equal); Writing – original draft (equal); Writing – review & editing (equal). **Michele Celebrano**: Data curation (equal); Formal analysis (equal); Writing – original draft (equal); Writing – review & editing (equal). **Marco Finazzi**: Data curation (equal); Formal analysis (equal); Funding acquisition (equal); Writing – original draft (equal); Writing – review & editing (equal). **Giovanni Pellegrini**: Data curation (equal); Formal analysis (equal); Writing – original draft (equal); Writing – review & editing (equal). **Paolo Biagioni**: Data curation (equal); Formal analysis (equal); Methodology (equal); Supervision (equal); Writing – original draft (equal); Writing – review & editing (equal). **Emiliano Descrovi**: Conceptualization (equal); Data curation (equal); Formal analysis (equal);

Methodology (equal); Writing – original draft (equal); Writing – review & editing (equal). **Matthieu Roussey**: Conceptualization (equal); Formal analysis (equal); Supervision (equal); Writing – original draft (equal); Writing – review & editing (equal). **Jari Turunen**: Conceptualization (equal); Funding acquisition (equal); Methodology (equal); Supervision (equal); Writing – original draft (equal); Writing – review & editing (equal).

DATA AVAILABILITY

The data that support the findings of this study are available from the corresponding author upon reasonable request.

APPENDIX A: INCIDENT PULSE CHARACTERISTICS

In Fig. 8, we show the characteristics of the incident pulse from our laser source when the central wavelength is set to 800 nm.

The FROG error was 0.0033 during the measurement, which can be considered quite low, indicating good convergence of the FROG retrieval algorithm. Visually, it can be realized by comparing the measured and retrieved FROG spectrograms plotted in Figs. 8(a) and 8(b), respectively. From this measurement, we find that the spectral full width at half-maximum (FWHM) is 11.37 nm; Fig. 8(c) and the temporal FWHM is 104 fs (of the intensity profile); Fig. 8(d). This FWHM corresponds to $T = 88$ fs, according to Eq. (1). From the retrieved phase profiles, one can also find that the pulses from the laser source are almost bandwidth limited. We have used this spectral information throughout our theoretical investigations or simulations, except in the case in Fig. 4.

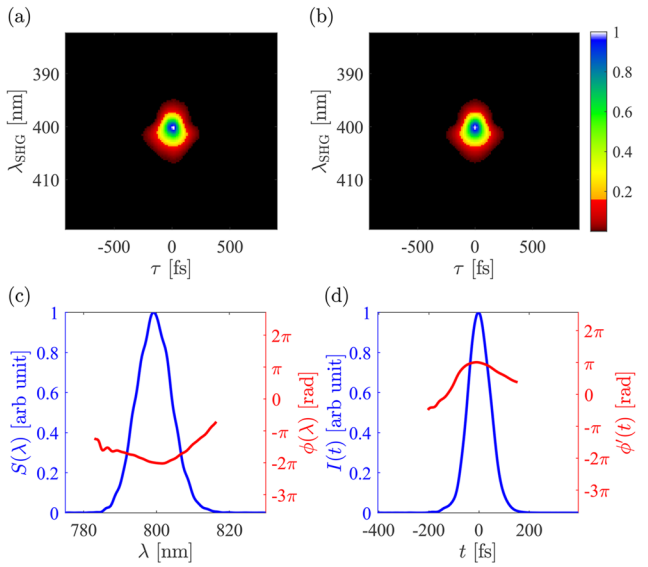

FIG. 8. (a) Measured and (b) retrieved SHG FROG spectrograms of the incident pulse, directly from the laser source, with $N \times N = 128 \times 128$ pixel resolution: FROG error of 0.0033. In the lower row, we show (c) retrieved spectral and (d) temporal intensity profiles with phase (in red) profiles, respectively.

APPENDIX B: CONNECTION BETWEEN THE FIELD CROSS-CORRELATION AND VISIBILITY

Let us consider TE polarization and denote the incident and reflected temporal plane-wave pulses propagating in the direction of the base ray by $E_i(t)$ and $E_r(t)$. Furthermore, we assume an interferometric setup that forms a superposition of the time-delayed incident (reference) pulse and the reflected pulse, as in

$$E(t;\tau) = E_i(t+\tau) + E_r(t). \tag{B1}$$

An ideal square-law detector would measure a temporal interference pattern,

$$I(t;\tau) = |E(t;\tau)|^2 = I_i(t+\tau) + I_r(t) + 2\Re\left[E_i^*(t+\tau)E_r(t)\right], \tag{B2}$$

while a slow detector gives the time integral,

$$I(\tau) = \int_{-\infty}^{\infty} I(t;\tau)\mathrm{d}t = I_i + I_r + 2\Re[C(\tau)], \tag{B3}$$

where

$$C(\tau) = \int_{-\infty}^{\infty} E_i^*(t+\tau)E_r(t)\mathrm{d}t. \tag{B4}$$

If the stack has no loss, we have $I_r = I_i$.

Using the envelope representations $E_i(t) = A_i(t)\exp(-i\omega_0 t)$ and $E_r(t) = A_r(t)\exp(-i\omega_0 t)$, assuming that the incident field is a transform-limited Gaussian pulse with $A_i(t) = A_i \exp\left(-t^2/T^2\right)$, and representing the envelope of the reflected pulse in terms of its amplitude $A_r(t)$ and phase $\alpha_r(t)$, the cross-correlation in Eq. (B4) takes the form

$$C(\tau) = A(\tau)\exp(-i\omega_0\tau), \tag{B5}$$

where

$$A(\tau) = A_i^* \int_{-\infty}^{\infty} |A_r(t)| \exp\left[-\frac{(t+\tau)^2}{T^2}\right] \exp\left[i\alpha_r(t)\right]\mathrm{d}t. \tag{B6}$$

We can now insert the envelope field given by the stratified-medium theory in this expression and integrate it numerically.

We are interested in recovering the envelope $A(\tau)$ of the cross-correlation function $C(\tau)$ in Eq. (B3). To this end, it is useful to express the envelope in terms of its amplitude $|A(\tau)|$ and phase $\gamma(\tau) = \arg[A(\tau)]$ as

$$A(\tau) = |A(\tau)|\exp[i\gamma(\tau)]. \tag{B7}$$

Doing so, Eq. (B3) gives (assuming that there is no loss)

$$I(\tau) = 2I_i\{1 + |A(\tau)|\cos[\gamma(\tau) - \omega_0\tau]\}. \tag{B8}$$

We, therefore, have an interference pattern that varies in the τ scale at the central optical frequency ω_0, showing maxima I_{max} and minima I_{min} when τ is scanned in fine scale (corresponding to a z scan over a few central wavelengths). This can be accomplished by a piezo stage for any central value of the delay, controlled by a long-range translation stage. The phase $\gamma(\tau)$ shows up in the positions of the fringes, whereas the local visibility,

$$V(\tau) = \frac{I_{max} - I_{min}}{I_{max} + I_{min}} = |A(\tau)| \tag{B9}$$

of the pattern gives the amplitude.

REFERENCES

[1] W. M. Robertson and M. S. May, "Surface electromagnetic wave excitation on one-dimensional photonic band-gap arrays," Appl. Phys. Lett. **74**, 1800–1802 (1999).

[2] M. Liscidini and J. E. Sipe, "Enhancement of diffraction for biosensing applications via Bloch surface waves," Appl. Phys. Lett. **91**, 253125 (2007).

[3] F. Villa and J. A. Gaspar-Armenta, "Photonic crystal to photonic crystal surface modes: Narrow-bandpass filters," Opt. Express **12**, 2338–2355 (2004).

[4] E. Mogni, G. Pellegrini, J. Gil-Rostra, F. Yubero, G. Simone, S. Fossati, J. Dostálek, R. Martínez Vázquez, R. Osellame, M. Celebrano, M. Finazzi, and P. Biagioni, "One-dimensional photonic crystal for surface mode polarization control," Adv. Opt. Mater. **10**, 2200759 (2022).

[5] B. Vosoughi Lahijani, N. Descharmes, R. Barbey, G. D. Osowiecki, V. J. Wittwer, O. Razskazovskaya, T. Südmeyer, and H.-P. Herzig, "Centimeter-scale propagation of optical surface waves at visible wavelengths," Adv. Opt. Mater. **10**, 2102854 (2022).

[6] F. Giorgis, E. Descrovi, C. Summonte, L. Dominici, and F. Michelotti, "Experimental determination of the sensitivity of Bloch surface waves based sensors," Opt. Express **18**, 8087–8093 (2010).

[7] A. Sinibaldi, N. Danz, E. Descrovi, P. Munzert, U. Schulz, F. Sonntag, L. Dominici, and F. Michelotti, "Direct comparison of the performance of Bloch surface wave and surface plasmon polariton sensors," Sens. Actuators, B **174**, 292–298 (2012).

[8] A. A. Popkova, A. A. Chezhegov, M. G. Rybin, I. V. Soboleva, E. D. Obraztsova, V. O. Bessonov, and A. A. Fedyanin, "Bloch surface wave-assisted ultrafast all-optical switching in graphene," Adv. Opt. Mater. **10**, 2101937 (2022).

[9] D. A. Shilkin, E. V. Lyubin, and A. A. Fedyanin, "Nonlinear excitation and self-action of Bloch surface waves governed by gradient optical forces," ACS Photonics **9**, 211–216 (2022).

[10] A. L. Asilevi, H. Pesonen, S. Pelisset, E. Descrovi, M. Roussey, and J. Turunen, "Pulse modulation by Bloch surface wave excitation," Opt. Lett. **47**, 2574–2577 (2022).

[11] R. Trebino, *Frequency-Resolved Optical Gating: The Measurement of Ultrashort Laser Pulses* (Springer Science & Business Media, 2000).

[12] D. Show, A. Halder, T. K. Hakala, and M. Koivurova, "Single-shot measurement of overall degree of spectral coherence: Bulk-generated supercontinuum case," Phys. Rev. B **105**, 104310 (2022).

[13] R. Ali, M. R. Saleem, M. Roussey, J. Turunen, and S. Honkanen, "Fabrication of buried nanostructures by atomic layer deposition," Sci. Rep. **8**, 15098 (2018).

[14] H. B. Profijt, S. E. Potts, M. C. M. van de Sanden, and W. Kessels, "Plasma-assisted atomic layer deposition: Basics, opportunities, and challenges," J. Vac. Sci. Technol., A **29**, 050801 (2011).

[15] M. Häyrinen, M. Roussey, A. Bera, M. Kuittinen, and S. Honkanen, "Atomic layer re-deposition for nanoscale devices," in *Encyclopedia of Plasma Technology* (CRC Press, 2016).

[16] J. A. Woollam, B. D. Johs, C. M. Herzinger, J. N. Hilfiker, R. A. Synowicki, and C. L. Bungay, "Overview of variable-angle spectroscopic ellipsometry (VASE): I. Basic theory and typical applications," Proc. SPIE **10294**, 3–28 (1999).

[17] V. Liu and S. Fan, "S^4: A free electromagnetic solver for layered periodic structures," Comput. Phys. Commun. **183**, 2233–2244 (2012).

[18] F. Fortin, F.-M. De Rainville, M.-A. Gardner, M. Parizeau, and C. Gagné, "DEAP: Evolutionary algorithms made easy," J. Mach. Learn. Res. **13**, 2171–2175 (2012).

[19] J. M. Dudley, G. Genty, and S. Coen, "Supercontinuum generation in photonic crystal fiber," Rev. Mod. Phys. **78**, 1135–1184 (2006).